ISSN 1392–1320 MATERIALS SCIENCE (MEDŽIAGOTYRA). Vol. 28, No. 2. 2022

Adsorption of Azo Dye on Magnetically Separable Fe_3O_4/CeO_2 Nanocomposite: Kinetics, Isotherm, Mechanism

Zhihao AN [1], Wenwen ZHANG [2], Jingying MA [1], Ke ZENG [1], Ming YUAN [1], Donghui CHEN [2] *

[1] *College of Chemical and Environmental Engineering, Shanghai Institute of Technology, Shanghai 201418*
[2] *College of Environmental Science and Engineering, Donghua University, Shanghai 201620*

crossref http://dx.doi.org/10.5755/j02.ms.28019

Received 19 November 2020; accepted 15 March 2021

In this study, magnetically separable Fe_3O_4/CeO_2 nanocomposite (F/CNc) was first synthesized in hydrothermal and sol-precipitation methods and characterized by techniques including SEM-EDS, XRD, BET, FT-IR and VSM. The adsorption experiments of acid black dye (AB210) onto F/CNc were carried out under the conditions of temperature (30 – 60 °C), solution pH (1 – 11), Fe-Ce molar ratio (1:2.5 – 4) and initial dye concentrations (20 – 80 mg/L). The adsorption capacity of AB210 increased with increasing initial dye concentration and temperature, and decreased with increasing solution pH. The maximum adsorption capacity of F/CNc for AB210 reached 124.5 mg/g when Fe-Ce molar ratio was 1:3. Pseudo-first-order and pseudo-second-order models were then used to describe the kinetics of adsorption, of which the latter fitted the adsorption process well, and the adsorption process complied also with the intra-particle diffusion model. The isothermal adsorption was described using Langmuir, Freundlich and Temkin models and the Langmuir model matched. FT-IR and Zeta-potential measurement proved the physical adsorption process of AB210 onto F/CNc. The saturation magnetizations of Fe_3O_4 nanospheres and F/CNc were measured to be 69.1 emu/g and 22.9 emu/g respectively, indicating the coating layer reduced the magnetization of Fe_3O_4 nanospheres, but F/CNc were still separated easily by applying a magnetic field, keeping easy separability. Being easy to recover and remaining adsorption efficiency 90 % in comparison to the original even after four adsorption cycles, demonstrate the effectiveness and practical application of F/CNc as an adsorbent.

Keywords: Fe_3O_4/CeO_2, acid black, adsorption mechanism, separation.

1. INTRODUCTION

Industrialization has rapidly accelerated, which resulted in increasing emission of organic pollutants like dyestuff in water [1]. Azo dyes possess 70 % of the total dyestuffs used in the textile [2], paper and leather industries [3]. They belong to the class of aromatic and heterocyclic compounds consisting of azo bond, which limits the removal effect in dye wastewater treatment [3]. Over the past years, many physical and chemical technologies including adsorption [4], advanced oxidation process [5], photocatalysis [6] and biological treatment [7] have been developed for the dye wastewater treatment, and have their advantages and disadvantages [8]. Among these technologies, the adsorption process is an efficient and economical one for removing azo dyes from wastewater [9].

In adsorption respect, adsorbent is the key factor. Cerium oxide (CeO_2), being one of the well-known rich and cheap rare earth oxides, has excellent thermal stability, optical properties, and oxygen ion transport capacity, which have attracted attention from scholars and brought its wide application in numerous fields, as adsorbents [10], catalysts [11], oxygen sensors [12], ultraviolet blocking material [13] and others [14, 15]. Specially, as a high-performance adsorbent in the field of sewage treatment, CeO_2 has been used to remove a variety of harmful anion dyes. Oman [16] demonstrated a new approach for the efficient removal of anionic organic dyes from wastewater using nanostructured CeO_2 in which its adsorption capacity for Acid orange10 and Congo red reached 14.53 and 14.03 mg. g^{-1} respectively. Wu [17] described the adsorption behaviour of CeO_2 nanotubes for Congo red, and confirmed that the Congo red was successfully coated on the surface of CeO_2 nanotubes by electrostatic attraction.

Unfortunately, the adsorbents are not easy to separate from the solution. Furthermore, most of them were discarded together with sludge after wastewater treatment, and causing secondary pollution. In contrary, magnetic adsorbents can be easily separated from the liquid phase by simply applying a magnetic field and have been developed to remove dyes in wastewater [18, 19]. In recent years, researchers have combined the Fe_3O_4 with the adsorbent. Cheng [20] synthesized magnetic graphene oxide/vinyl alcohol composite gels, which exhibited convenient magnetic separation capability, and the adsorption capacity for methylene blue dye reached 85.63 mg/g. In our preview work [21, 22], block-shaped Fe_3O_4/CeO_2 nanocomposite was prepared and the adsorption capacity for dye reached 90.5 mg/g. In this research, we have prepared spherical F/CNc, to increase specific surface area and enhance adsorption capacity. Furthermore, we have studied the adsorption mechanism of F/CNc for dye.

In this paper, magnetically separable F/CNc was firstly synthesized in hydrothermal and sol-precipitation methods, and characterized by techniques including SEM-EDS, XRD, BET, FT-IR and VSM. In adsorption experiments of

* Corresponding author. Tel.: +86-021-60871326; fax: +86-021-60871326. E-mail address: *chendh@dhu.edu.cn* (D. Chen)

AB210 onto F/CNc, the effects of initial dye concentration, pH, temperature and Fe-Ce molar ratio on the adsorption were investigated. In order to understand the adsorption mechanism, pseudo-first-order and pseudo-second-order kinetic models were used to describe the kinetics of adsorption and the adsorption process complied also with the intraparticle diffusion model. The isothermal adsorption was described using Langmuir, Freundlich and Temkin models. The thermodynamic parameters of the adsorption process, such as Gibbs free energy ($\Delta G°$), enthalpy ($\Delta H°$) and entropy ($\Delta S°$) changes were determined by using the isothermal data of the adsorption process. The zeta potential, FT-IR measurement and model-fitting method was used to analyze the coexistence and mechanism of phase transformation. Furthermore, the saturation magnetizations of Fe_3O_4 nanospheres and F/CNc were measured by vibrating sample magnetometer (VSM), and the recyclability of F/CNc was also examined.

2. EXPERIMENTAL

2.1. Chemicals

Materials were purchased from Shanghai Titan Science Co., Ltd.: cerium nitrate hexahydrate (99 %), ethylene glycol (AR), sodium acetate (AR), polyethylene glycol (AR), ferric chloride hexahydrate (AR), ammonia (25 % – 28 %), ethanol (AR), polyethylene glycol (AR). Azo black dye (AB210) was purchased from Alibaba and its chemical structure is shown in Fig. 1. The double distilled water (DI) used in the experiment was provided by the school laboratory.

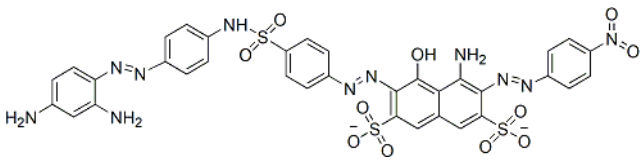

Fig. 1. The chemical structure of acid black (AB210)

2.2. Preparation of Fe_3O_4/CeO_2 nanocomposite

Fe_3O_4 nanospheres were synthesized via hydrothermal method [23]. First, 2.7 g ferric chloride hexahydrate was added into 80 ml ethylene glycol under vigorous stirring. Then, 7.2 g sodium acetate and 2.0 g polyethylene glycol were added into above solution. After stirring about 30 minutes, the mixed solution was transferred to a Teflon-lined (100 ml) for 10 hours at 200 °C. The obtained Fe_3O_4 microspheres were washed with double distilled water and ethanol for twice times, then dried at 60 °C overnight.

The method of CeO_2 nanoparticles coated surface of Fe_3O_4 nanospheres was as follows [21]: 50 mg Fe_3O_4 nanospheres obtained above were added into double distilled water (100 ml), ultrasonically dispersed for 10 minutes, and vigorously stirred at 65 °C. After stirring about 30 minutes, 5 ml cerium nitrate hexahydrate (0.1 mol/L) was added into the solution, and stirred 30 minutes. Ammonic water was added to allow the solution keeping neutral. After stirring 30 minutes, they were collected with magnet, washed twice with distilled water and alcohol, finally dried at 80 °C for 10 hours to get Fe_3O_4/CeO_2 nanocomposite (F/CNc).

2.3. Material characterization

The crystal structure and phase of the sample were determined by X-ray diffractometer (XRD, Mini Flex600, Rigaku), the morphology and microstructure of the sample were observed using field emission scanning electron microscope at 3.0 kV, and the element distribution in the sample was captured by a tracer electron microscope-energy spectrometer (SEM-EDS), (SEM:JSM-5600LV; EDS:IE300X).The chemical bonds of the sample was measured using Fourier infrared spectroscopy (FT-IR:WQF-520), and the hysteresis loop of the sample were measured by a vibrating sample magnetometer (VSM 7407). The specific surface area and pore size distribution of the sample were determined by a nitrogen adsorption-desorption instrument (Micrometrics Tristar 3000). The Zata potential were determined by a Zatasizer Nano ZSP.

2.4. Evaluation of adsorption performance

The adsorption experiments were carried out using acid black dye (AB210) as model organic dye pollutant. The conical flask containing the dye solution was wrapped with aluminum foil, and AB210 was stirred in a dark box to prevent the interference of photocatalysis. 50 mg F/CNc was added into 100 mL of AB210 solution. After ultrasonic dispersion 10 min, placed it in a dark box and kept stirring. Sampling was carried out in sequence at an interval of 20 minutes, the supernatant was taken with a pipette, and the absorbance was measured by taking its UV–vis absorption spectra at 462 nm wavelength of maximum absorption. The effects of the Fe-Ce molar ratio (1:2 – 4), initial concentration (20 – 80 mg/L), temperature (30 – 60 °C), and pH (1 – 11) on the adsorption performance were investigated. The desired pH value of the adsorption medium was achieved by use of 0.1 M HCl and 0.1 M NaOH solutions through a check using pH meter.

The adsorption capacity (Q_e), and the adsorption efficiency (%) for AB210 were calculated using the following equations:

$$Q_e = \frac{(C_0 - C_e)}{M}; \quad (1)$$

$$\text{Adsorption efficiency (\%)} = \frac{(C_0 - C_e)\times 100}{C_0}, \quad (2)$$

where C_o (mg/L) and C_e (mg/L) are the initial and equilibrium concentration of adsorbate, M (gram) is the weight of adsorbent, and V (L) is the volume of the solution [24, 25].

3. RESULTS AND DISSUSSION

3.1. Morphology

The morphologies of Fe_3O_4 nanosphere and F/CNc were analyzed by SEM-EDS. In Fig. 2 a and b, spherical particles Fe_3O_4 with uniform distribution were observed and their mean diameter was found as 400 nm.

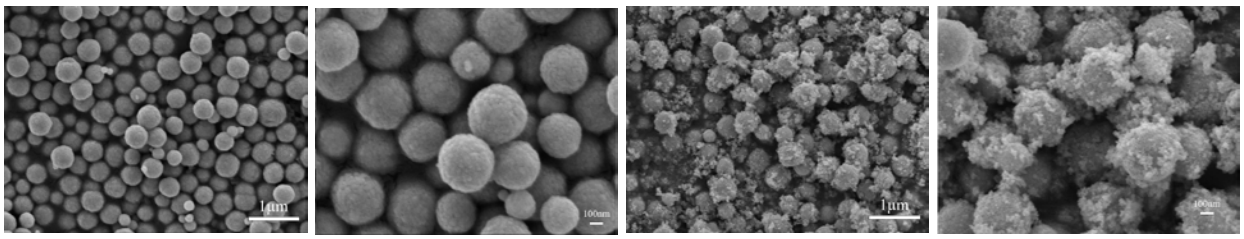

a b c d

Fig. 2. FE-SEM images: a, b – Fe_3O_4; c, d – F/CNc

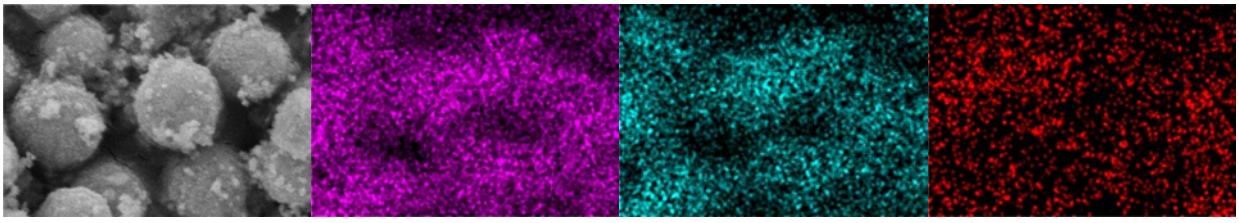

a b c d

Fig. 3. SEM: a – F/CNc; corresponding EDS elemental mapping for elements: b – O; c – Ce; d – Fe

In addition, there were still a few gaps on the surface of Fe_3O_4 nanospheres, indicating that CeO2 nanoparticles were not uniformly coated on the surface of Fe_3O_4 nanospheres. The EDS element map Fig. 3 b – d, corresponding to the SEM Fig. 3 a of F/CNc, confirmed the coexistence of O, Ce and Fe in the prepared F/CNc. The results were in agreement with XRD findings, which further proved that CeO_2 were successfully coated on Fe_3O_4 nanospheres. It is obviously that we have successfully prepared spherical F/CNc with uniform morphology while F/CNc in our previous work was block morphology.

3.2. Powder X-ray diffraction

X-ray diffraction (XRD) was performed to investigate the phase structure of F/CNc. XRD of pristine Fe_3O_4 and CeO_2 were also analyzed as standard samples for comparison. It was observed from Fig. 4 that the XRD pattern of F/CNc matched with the combination of XRD of CeO_2 and Fe_3O_4.

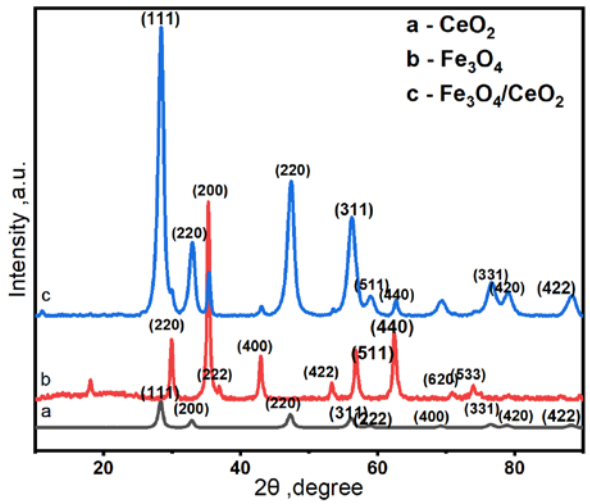

Fig. 4. XRD patterns of CeO_2, Fe_3O_4 and F/CNc

The 2θ values of Fe_3O_4 nanospheres were observed at 30.1°(220), 35.4°(311), 43.0°(400), 57.0°(511) and 62.5°(440), which confirmed well with standard XRD pattern of Fe_3O_4 (JCPDS NO.19-0629) [26]. Meanwhile, the 2θ values of CeO_2 nanoparticles were observed at 28.55°(111), 33.08°(200), 47.48°(220) and 56.33°(311), which confirmed well with standard XRD pattern of CeO_2 (JCPDS NO.34-0394) [27]. The diffraction peaks of F/CNc were found to be the superposition of those peaks from single Fe_3O_4 and pure CeO_2 and were observed at 2θ values 30.1°, 47.48° and 35.4° with more sharpened peaks. This observation was indicative of increased crystallinity amongst F/CNc. Such an increase in the crystallinity can be considered to be attributable to the exist of interactions between CeO_2 and Fe_3O_4. It can be supposed that the insertion of Fe atoms, arising from the reduction of Fe_3O_4 during pyrolysis, into the crystal lattice of CeO_2 [28].

3.3. Specific surface area and porosity

The surface area plays a key role in adsorption as it leads to number of active sites on the adsorbent. Fig. 5 illustrated the nitrogen adsorption-desorption isotherms curve for F/CNc.

According to the classification of the International Union of Pure and Applied Chemistry (IUPAC) (IUPAC, 1985) [29], the curve represented a type-IV curve with H3 hysteresis loop and was indicative of mesoporous behaviour. No peaks were detectable in the adsorption curve, indicating that there were not specific holes. Furthermore, the specific surface area of F/CNc was 69.0121 m^2/g, larger than that of CeO_2 nanoparticles 33.52 m^2/g [30]. The BJH average pore size was 10.1349 nm and the pore volume 0.21115 cm^3/g. F/CNc provided more adsorption sites for dye adsorption.

3.4. Magnetic properties

In this study, it was necessary to examine the change of magnetic properties between Fe_3O_4 nanospheres and F/CNc. Fig. 6 shows the magnetic properties of Fe_3O_4 nanospheres

and F/CNc measured using vibrating sample magnetometer (VSM) at room temperature. The two materials were superparamagnetic.

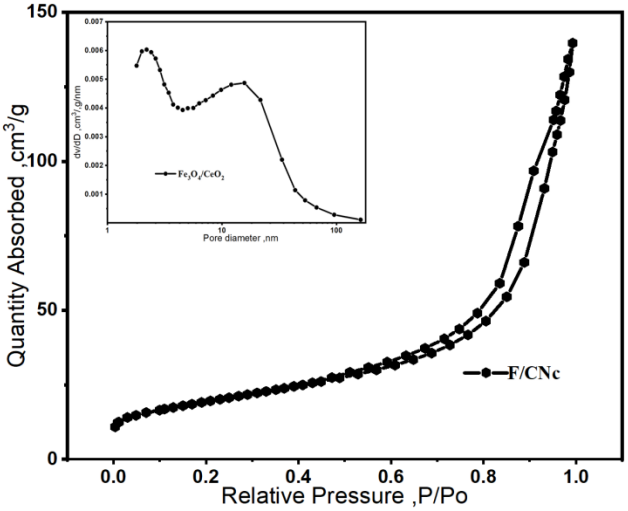

Fig. 5. Nitrogen adsorption-desorption isotherm of F/CNc. Inset: Corresponding BJH desorption, pore width size vs. pore volume

From Fig. 6, the saturation magnetizations of Fe_3O_4 nanospheres and F/CNc were obtained to be 69.1 emu/g and 22.9 emu/g respectively. Although the coating layer significantly reduced the magnetization of Fe_3O_4 nanospheres, as shown in inset of Fig. 6, F/CNc can be rapidly separated from the mixture within 3 s using a magnet after adsorption of AB210 in dye wastewater. This proved F/CNc is convenient for cyclic utilization and practical application.

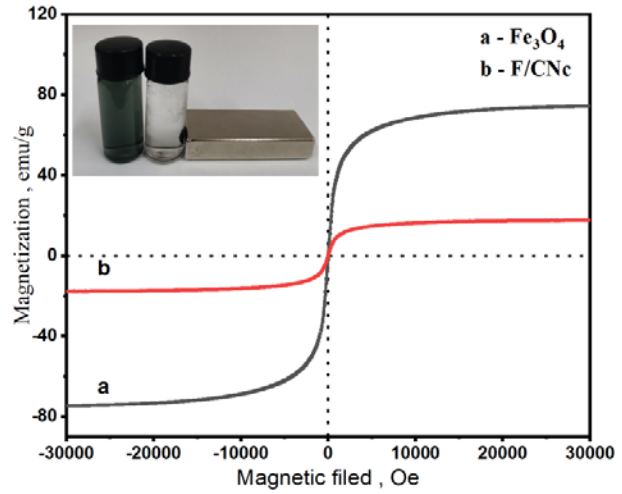

Fig. 6. Magnetic hysteresis loops of Fe_3O_4 nanosphere and F/CNc. Inset: separation of F/CNc by external magnet

3.5. Adsorption tests

3.5.1. Effect of molar ratio of Fe_3O_4 to CeO_2

As shown in Fig. 7, at molar ratio 1:3, F/CNc had the best adsorption effect on AB210 although the effect of molar ratio did not demonstrated significantly. Since the radius of Fe_3O_4 nanospheres and CeO_2 nanoparticles were 200 nm and 3.5 nm respectively, it was obvious by a simple calculate that about 3200 CeO_2 nanoparticles were needed to coat whole surface of a Fe_3O_4 nanosphere in the way of monolayer. Thus, when 1 mol Fe_3O_4 nanospheres were wrapped with 2.9 mol CeO_2 nanoparticles, whole surface of the Fe_3O_4 nanospheres would be coated by those CeO_2 nanoparticles just in monolayer, being close to molar ratio 1:3 of the adsorption test and providing the most adsorptive sites theoretically. At r = 1:2 or 2.5, CeO_2 nanoparticles could not completely coat whole surface of Fe_3O_4 nanospheres and the adsorptive sites on F/CNc were less than those at r = 1:3, resulting in less adsorption effect. At r = 1:4, the adsorption effect of F/CNc was less than that at r = 1:3, perhaps due to the thick covering of CeO_2 shell layer on the surface of Fe_3O_4 microspheres, leading to no increase of adsorptive sites.

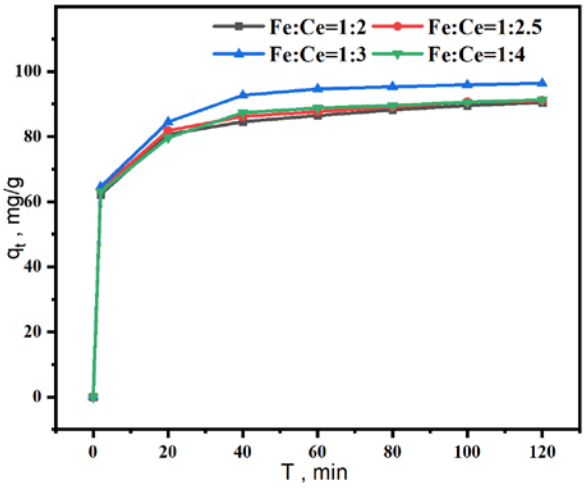

Fig. 7. Effect of molar ratio of CeO_2 to Fe_3O_4 on adsorption

3.5.2. Effect of solution pH

Both adsorbant and adsorbent have functional groups that can be protonated or deprotonated, which results in electrostatic attraction or repulsion between the charged adsorbant and the adsorbent [31]. Since the surface charge of adsorbent as well as the charge of dye in solution depend greatly on the pH of the solution, the effect of pH on adsorption of AB210 was studied. The series of adsorption tests were carried out at different pH values ranging from 1 to 11. As shown in Fig. 8 a, the removal of AB210 increased from pH 7 down pH 1, but reduce from pH 9 to pH 11 observably. This phenomenon can be explained by electrostatic adsorption. The role of surface charge towards adsorption was examined by Zatasizer Nano ZSP, and the zeta potential and equilibrium adsorption capacity of F/CNc at different pH were shown in Fig. 8 b. The both of zeta potential and equilibrium adsorption capacity decreased with the increase of initial pH. When the charge of adsorbent in the solution becomes zero, the pH is called pH_{pzc}, and the pH_{pzc} was obtained to be 7.7 (shown in Fig. 8 b). While $pH < pH_{pzc}$, the surface of F/CNc had a net positive charge. Once $pH > pH_{pzc}$, the surface had a net negative charge. AB210 is an anionic dye which cannot adsorb onto F/CNc. At an acidic pH, the hydroxyl group (-OH) onto the surface of F/CNc was protonated into a cationic form ($-OH^{2+}$), and generates electrostatic attraction with anionic dyes. Therefore, when the pH was larger than pH_{pzc}, the adsorption of F/CNc onto AB210 was efficient. However,

under alkaline pH conditions, the hydroxyl group (-OH) was deprotonated into an anionic form ($-O^-$), reducing the number of positively charged sites [22]. Such an environment was not conducive to the adsorption of negatively charged dye molecules. Therefore, when the pH increased, the adsorption capacity of F/CNc on AB210 decreased, due to the electrostatic repulsion between the negatively charged sites on the surface of F/CNc and the negatively charged dye molecules AB210. The changes of surface charge with pH in this study are consistent with Jone·s research [32].

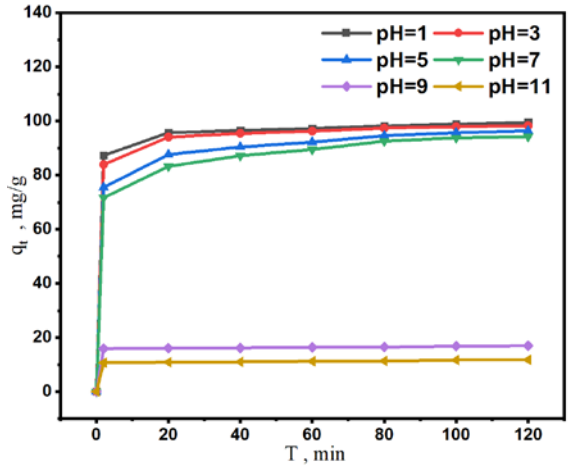

a

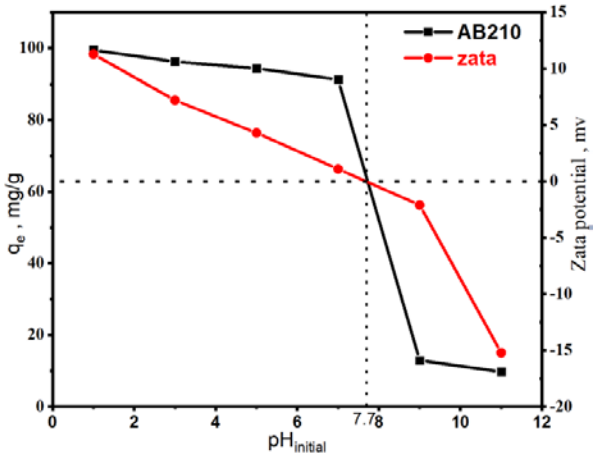

b

Fig. 8. a – effect of pH on adsorption; b – zeta potential and equilibrium adsorption capacity

3.5.3. Effect of initial dye concentration

The initial concentration of dye provides an important driving force for the transfer of dye molecules between the liquid and solid phases. In order to investigate the effect of the initial dye concentration on the adsorption, the adsorption experiments were carried out at T = 303 K, pH = 7, and the initial dye concentration among 20 to 80 mg· L^{-1}. The results were represented in Fig. 9. When the initial concentration of AB210 dye changed from 20 to 70 mg·L^{-1}, there was a monotonic increase in the adsorption of F/CNc. But at the initial concentration of 80 mg·L^{-1}, the adsorption capacity did not persistently increased, indicating the adsorption of F/CNc reached saturation. As shown in Fig. 9, the q_e gradually increased as the stirring time increased and finally reached an equilibrium state. In the first 20 minutes, the adsorption rate of AB210 molecules by F/CNc was faster. The possible reason was many unoccupied spots on the surface of F/CNc in the initial stage, but AB210 molecules gradually were adsorbed on the surface of F/CNc as the time increased, and then slowly entered the voids of F/CNc. This process led to a continuous decrease in the adsorption rate.These results were consistent with the results of using CaO/CeO_2 composite to adsorb acid orange 7 dye reported by Thirunavukkarasu et al [33].

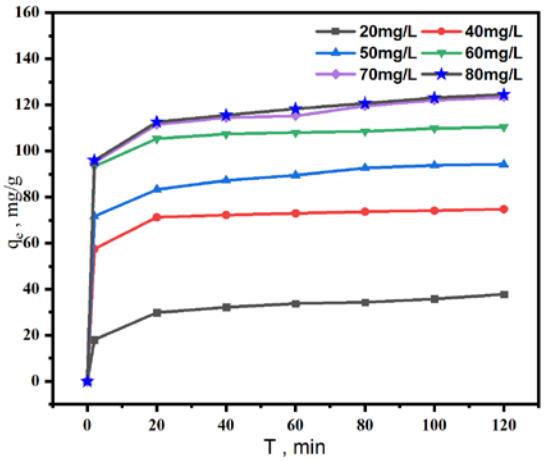

Fig. 9. Effect of initial AB210 concentration on adsorption of F/CNc

3.6. Regenerate study

The recyclability is very important for adsorbents in actual application. In order to investigated the recyclability of F/CNc, the adsorption and desorption cycle was repeated four times. After adsorption test, desorption was carried out. Firstly F/CNc collected by magnet and dried at 60 °C for 2 h. The regenerated F/CNc was used as an adsorbent to retest the adsorption performance.

As shown in Fig. 10, the removal efficiency for the first cycle of the adsorption process reached 92 % and it slightly decreased to 89.34 %, 85.63 % and 81.12 % for the second, third and fourth cycle respectively.

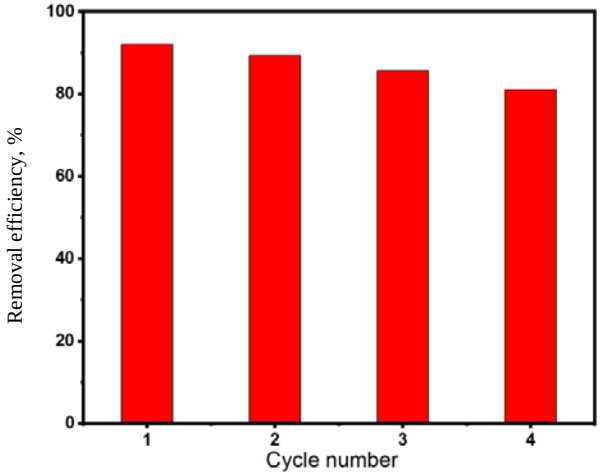

Fig. 10. Recyclability of F/CNc

The adsorption efficiency lost about 10 %, similar to that of our preview work [21]. The data showed the good regeneration ability and reusability of the adsorbent making it competent for water treatment.

3.7. Adsorption kinetics

The adsorption process depends on contact time between dye molecules and adsorbent. So, the effect of contact time on adsorption capacity was studied using kinetic models. The data of AB210 adsorption experiment in Fig. 9 were fitted by three kinetic models: pseudo-first-order, pseudo-second-order and intra-particle diffusion respectively:

$$\ln(q_e-q_t)=\ln(q_e)-k_1 t; \quad (3)$$

$$\frac{t}{q_t}=\frac{1}{k_2 q_e^2}+\frac{t}{q_e}; \quad (4)$$

$$q_t=k_p t^{0.5}+C, \quad (5)$$

where k_1 (min^{-1}) is pseudo-first-order adsorption rate constant, k_2 ($mg\cdot g^{-1}\cdot min^{-1}$) is pseudo-second-order adsorption rate constant, k_p ($mg\cdot g^{-1}\cdot min^{-0.5}$) is intra-particle diffusion rate constant, C ($mg\cdot g^{-1}$) is a constant [34] and q_t ($mg\cdot g^{-1}$) is the amounts of adsorbate adsorbed at different time intervals.

As shown in Fig. 11 a and b, the data at the concentrations among 20 $mg\cdot L^{-1}$ to 80 $mg\cdot L^{-1}$ were fitted by pseudo-first-order adsorption and pseudo-second-order adsorption model respectively, and there was a good agreement between the experimental $q_{e,exp}$ and the calculated one obtained from pseudo-second-order model. Based on the correlation coefficient (R^2) shown at Table. 1, it was higher for pseudo-second-order kinetic model. All these results suggested that the adsorption process followed pseudo-second-order model. The pseudo-second-order rate constants K_2 for AB210 onto F/CNc indicated a steady increase with initial dye concentration. The involved driving force was the mass gradient which increased with an increase in the concentration. At lower concentrations, the ratios of dye molecules to the adsorption sites were low. Hence, there was a possibility of only monolayer coverage but at higher concentration multilayer adsorption was more likely to happen.

Intra-particle diffusion was also fitted by the adsorption data of AB210. As shown in Fig. 11 c, there were two different stages in the adsorption process.

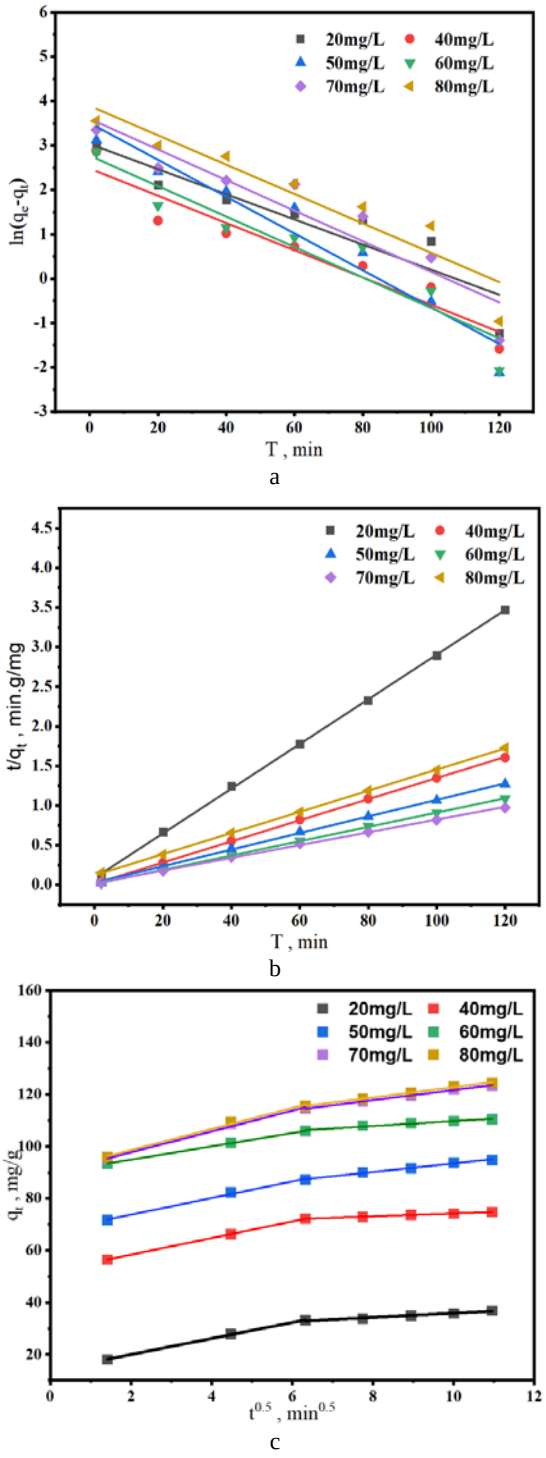

Fig. 11. Adsorption kinetic for adsorption of AB210 onto F/CNc: a – pseudo-first order; b – pseudo-second order; c – in-particle diffusion

Table 1. Parameters of pseudo-first-order, pseudo-second-order and in-particle diffusion model at different initial concentrations

Model	C_o, $g\cdot L^{-1}$	20	40	50	60	70	80
	$q_{e,exp}$, $mg\cdot g^{-1}$	37.826	74.762	94.258	110.4	123.362	124.486
Pseudo-first-order	k_1, min^{-1}	0.02833	0.03071	0.04151	0.03433	0.03499	0.03311
	R^2	0.8113	0.9006	0.9340	0.8788	0.8607	0.8668
Pseudo-second-order	k_2, $g\cdot mg^{-1}\cdot min^{-1}$	0.02819	0.01332	0.0271	0.00903	0.00804	0.01334
	R^2	0.9996	0.9998	0.9990	0.9998	0.9986	0.9999
Intra-particle diffusion	K_p, $mg\cdot g^{-1}\cdot min^{-0.5}$	0.78840	0.78840	2.20385	2.47496	2.89257	2.87468
	R^2	0.927	0.9627	0.9882	0.9861	0.9942	0.9898

The stage with a larger slope originated from the diffusion of AB210 through the solution onto the surface of F/CNc, and the stage with a smaller slope reflected adsorption rate reduction due to diffusion of AB210 into the voids of F/CNc. Similar results were observed in Congo red dye on porous CeO_2 nanotubes [17].

3.8. Adsorption isotherm

The adsorption isotherm of AB210 onto F/CNc was performed in order to analyzed the interaction between the adsorbate molecules and the sites of F/CNc. Langmuir, Freundlich and Temkin adsorption isotherm models were used to fit the equilibrium adsorption capacity Q_e by equations respectively:

$$Q_e = \frac{Q_m K_L C_e}{1+C_e K_L}; \quad (6)$$

$$Q_e = K_F C_e^{1/F}; \quad (7)$$

$$Q_e = \frac{RT}{b_T}\ln(K_T C_e), \quad (8)$$

where Q_e (mg/g) is the amount of AB210 dye adsorbed at equilibrium, C_e (mg/L) is the concentration of AB210 at equilibrium, Q_m (mg/g) is the maximum adsorption capacity, and K_L (L/mg) is Langmuir constant. K_F (mg/g) (L/mg)1/n is the Freundlich constant, F is the dimensionless constant. K_T (L/mg) is Temkin constant, T (K) is temperature, and b_T (J/mol) is heat of adsorption [35, 36].

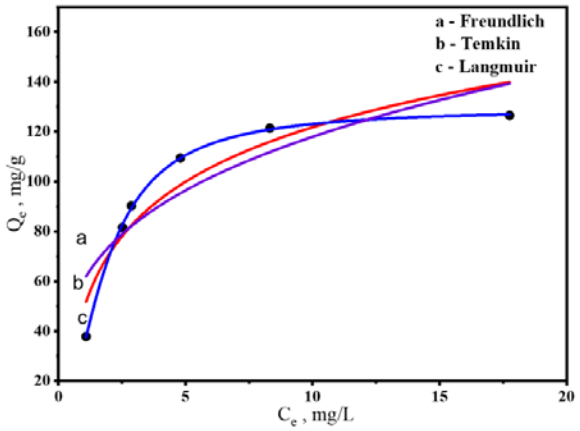

Fig. 12. Isotherms of AB210 adsorption onto F/CNc: a – Langmuir; b – Freundlich; c – Temkin

The fitted curves for Langmuir, Freundlich and Temkin isotherm models were represented in Fig. 12, indicating that Langmuir model fitted better. Correlation coefficients (R^2) of Langmuir model was higher than those of other models as shown in Table 2. It can be supposed that the adsorption process of AB210 onto F/CNc followed Langmuir isotherm model. Langmuir adsorption isotherm was applicable for monolayer coverage of the surface. The active sites were independent and can bind to a specific number of adsorbates. Concerned with Fig. 3, it can be seen that AB210 was adsorbed on the surface of F/CNc in monolayer. The maximum adsorption capacity was calculated by Langmuir model as 124.5 mg/g, which was considerably higher than other morphologies CeO_2 (Table 3). Moreover, the maximum adsorption capacity of F/CNc was 8.4 times than commercial CeO_2.

Table 2. Correlation coefficients R^2 of three isotherm models

Isotherm model	R^2
Langmuir isotherm	0.9991
Freundlich isotherm	0.7886
Temkin isotherm	0.8896

3.9. Thermodynamics study

Temperature is an important factor in controlling the adsorption process. The effect of solution temperature on the adsorption of AB210 by F/CNc was shown in Fig. 13 a.

Table 3. Maximum adsorption capacities of Ceria with different morphologies adsorbents to AB210 and other dyes

Adsorbents	Dyes	Q_m, mg/g	Reference
F/CNc	AB210	124.5	This work
Fe/Ce	AB210	90.50	Previous work
Commercial CeO_2	AB210	14.81	[22]
Ceria nanoparticles	AB210	35.29	[37]
Ceria nanofibers	Methyl Orange	10	[38]
nanostructured CeO_2	Acid orange10	14.53	[16]
nanostructured CeO_2	Congo red	14.03	[16]

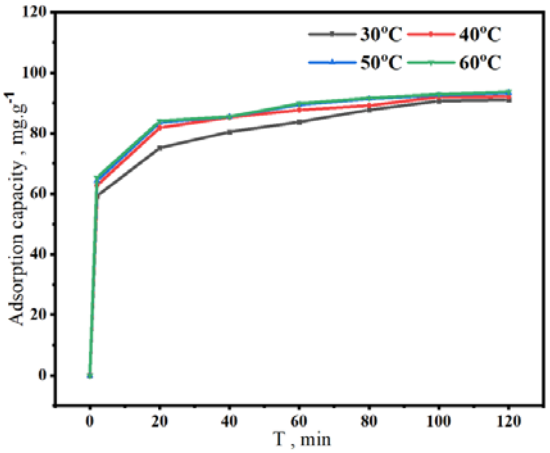

a

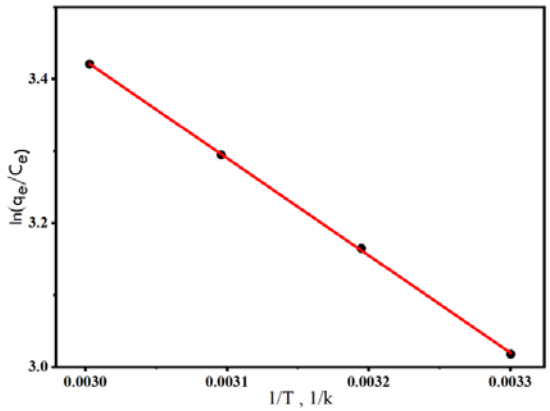

b

Fig. 13. a – thermodynamic diagram of adsorption of AB210 onto F/CNc; b – Van't Hoff

The adsorption capacity gradually increased with increase of temperature (30 – 60 °C), indicating that the adsorption process was mainly endothermic. The thermodynamic parameters, including Gibbs free energy change ($\Delta G°$), enthalpy ($\Delta H°$) and entropy ($\Delta S°$), were calculated according to:

$$ln(K_a) = \frac{\triangle S^0}{R} - \frac{\triangle H^0}{RT}; \quad (9)$$

$$\triangle G^0 = -RTln(K_a); \quad (10)$$

$$K_a = \frac{q_e}{c_e}, \quad (11)$$

where T(K) is the solution temperature, and K_a(L/g) is standard thermodynamic equilibrium constant defined by q_e/C_e. By plotting relationship between ln(k_a) and 1/T, the $\Delta H°$ and $\Delta S°$ values can be estimated from the slope and intercept [39].

By plotting ln(ka) vs 1/T in Fig. 13 b, three thermodynamic parameters data were obtained, shown in Table 3. The positive value of $\Delta H°$ (11.24 kJ·mol^{-1}) indicated that the adsorption process of AB210 onto F/CNc was an endothermic process. The positive value of $\Delta S°$ (62.20 J·mol^{-1}·K^{-1}) indicated that the randomness increased at the solid-liquid interface of AB210 onto F/CNc. With the increase of temperature, the value $\Delta G°$ decreased from –7.602 kJ·mol^{-1} to –9.388 kJ·mol^{-1}, indicating the feasibility and spontaneity of the adsorption process. In addition, this phenomenon also indicated that the adsorption process was more favourable at higher temperatures. Generally speaking, when the $\Delta G°$ value was in the range of –20 – 0 kJ·mol^{-1}, the adsorption process is essentially considered to be physical adsorption. If the $\Delta H°$ value is lower than 40 kJ·mol^{-1}, it conforms to the physical adsorption process [40]. Based on the obtained values of $\Delta H°$ and $\Delta G°$, the adsorption process of AB210 onto F/CNc was considered to be physical adsorption.

Table 4. Thermodynamic quantities for adsorption of AB210 onto F/CNc

T, °C	$\Delta G°$, kJ·mol^{-1}	$\Delta S°$, J·mol^{-1}·K^{-1})	$\Delta H°$, kJ·mol^{-1}	R^2
30	–7.602	62.20	11.24	0.9998
40	–8.209			
50	–8.981			
60	–9.388			

3.10. Adsorption mechanism

The interaction between AB210 and F/CNc was investigated by studying FT-IR. The comparison of FT-IR spectra of F/CNc before and after adsorption is shown in Fig. 14. Both peaks at 3439 cm^{-1} before adsorption and 3415 cm^{-1} after adsorption implied the stretching vibrations of O-H bond [41].

It was observed that the peak for stretching vibrations of O-H bond blue-shifted from 3439 to 3415 cm^{-1}. Both peaks at 1632 cm^{-1} and 1629 cm^{-1} implied the bending vibration of coordinated water [42] and the intensity of the latter increased also. These changes can be considered to be caused by forming hydrogen bonding with the dye molecule by O-H group of F/CNc. The peaks at 1342 cm^{-1} and 1046 cm^{-1} after adsorption were ascribed to the N-H bending vibration modes [10] belonged to AB210 molecule, which strongly proved that AB210 was adsorbed on the surface of F/CNc by hydrogen bond. Moreover, the peaks at 562 cm^{-1} and 633 cm^{-1} were the bending vibration of Ce-O and Fe-O bonds respectively [43, 44] but disappeared in the spectrum after adsorption. Hence, from both of zeta potential and FT-IR, it can be concluded that AB210 molecules was adsorbed on the surface of F/CNc by electrostatic attraction. Demonstrated in Fig. 15, AB210 molecules are dispersed in the solution.

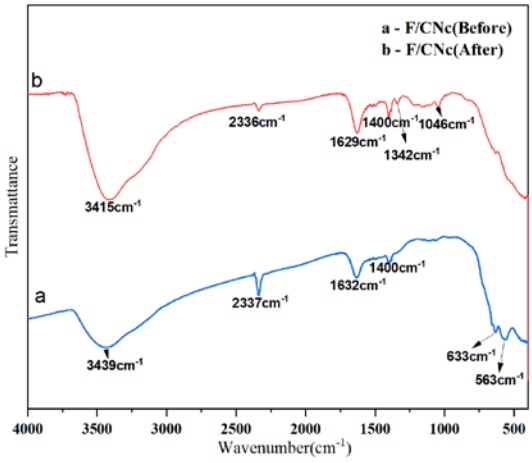

Fig. 14. FT-IR spectra of Fe_3O_4/CeO_2(F/CNc) before and after AB210 adsorption

Under acidic condition, the hydroxyl groups (-OH) on the surface of F/CNc are protonated into positively charged OH_2^{2+} groups, and AB210 molecules diffused to F/CNc particles through turbulent flow and then touched the surface.

With the accumulation of AB210 molecules on the surface, a small amount of AB210 molecules gradually enter the pores of F/CNc. Meanwhile, some AB210 molecules on the surface desorb into the solution, reaching the equilibrium state, coexistence of AB210 molecules adsorbed on the surface and desorbed in the solution. This process can be formulated as follows:

$$CeO_2\text{-}OH + H^+ \rightarrow CeO_2\text{-}OH^{2+}$$
$$CeO_2\text{-}OH^{2+} + C_{22}H_{14}N_6Na_2O_3\text{-}(SO_3)_2^{2-} \rightarrow$$
$$CeO_2\text{-}OH^{2\cdots}C_{22}H_{14}N_6Na_2O_3\text{-}(SO_3)_2^{2-}$$

4.CONCLUSIONS

It was developed a magnetically separable nanomaterial with sphere morphology using a simple and economical methods. The nanomaterial with specific surface area 69.0121 m^2/g and saturation magnetization 22.9 emu/g showed a very high separative behavior from the solution by applying a magnetic field and an adsorption capacity 124.5 mg/g towards azo dye. The maximum adsorption capacity of AB210 with F/CNc improved 1.38 times compared with our preview work. The adsorption process of anionic dye followed pseudo-second-order kinetics and the adsorption isotherm was described well by Langmuir isotherm model, signifying the homogeneous surface sites and monolayer uniform coverage of the adsorbate on the surface of the adsorbent.

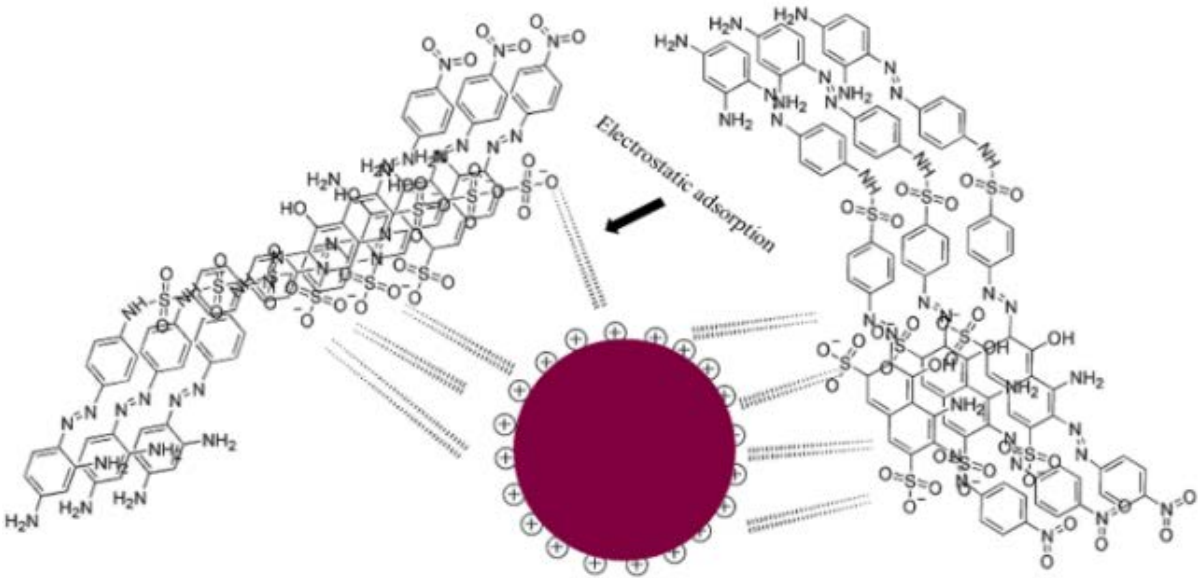

Fig. 15. Diagram of AB210 onto F/CNc

The adsorption mechanism was mainly electrostatic, which was confirmed by the pH effect, zeta potential measurement and FT-IR analysis. The adsorbent was easily regenerated up to four times just losing 10 % efficiency. As a new green adsorbent, the synthesized nanomaterial can be easily recovered in the applied magnetic field, which makes it easy to separate from the aqueous solution. Therefore, the synthesized nanomaterial has practical application in the removal of anionic dyes.

Acknowledgement

This research was funded by the Innovation Project of College Students Science and Technology offered by Shanghai Institute of Technology (No. DCX2019198).

REFERENCES

1. **Tatarchuk, T., Bououdina, M., Al-Najar, B., Bitra, R.B.** Green and Ecofriendly Materials for the Remediation of Inorganic and Organic Pollutants in Water *Applications in Water Technology* 10 2019: pp. 78 – 97. https://doi.org/10.1007/978-3-319-75484-04
2. **Goud B.S., Cha H.L.** Augmented Biodegradation of Textile Azo Dye Effluents by Plant Endophytes: A Sustainable, Eco-Friendly Alternative *Current Microbiology* 77 2020: pp. 3240 – 3255. https://doi.org/10.1007/s00284-020-02202-0
3. **Saratale, R.G., Gandhi, S.S., Purankar, M.V.** Decolorization and Detoxification of Sulfonated Azo Dye C.I. Remazol Red and Textile Effluent by Isolated Lysinibacillus sp. *Journal of Bioscience and Bioengineering* 115 2013: pp. 658 – 667. http://dx.doi.org/10.1016/j.jbiosc.2012.12.009
4. **Mohammad, A.T, Abdulhameed, A.S., Jawad, A.H.** Box-Behnken Design to Optimize the Synthesis of New Crosslinked Chitosan-glyoxal/TiO_2 Nanocomposite: Methyl Orange Adsorption and Mechanism Studies. *Journal of Biological Macromolecules.* 129 2019: pp. 98 – 109. https://doi.org/10.1016/j.ijbiomac.2019.02.025
5. **Gayathri, P.V., Yesodharan, S., Yesodharan, E.P.** Microwave/Persulphate Assisted ZnO Mediated Photocatalysis (MW/PS/UV/ZnO) as An Efficient Advanced Oxidation Process for the Removal of RhB Dye Pollutant from Water *Journal of Environmental Chemical Engineering* 7 2019: pp. 42 – 63. https://doi.org/10.1016/j.jece.2019.103122
6. **Malihe, K., Morasae, S., Elham, A., Yi, Z., Dong, C.Y., Zhang, J.L., Alireza, Z.** Well-designed Ag/ZnO/3D Graphene Structure for Dye Removal: Adsorption, Photocatalysis and Physical Separation Capabilities *Journal of Colloid and Interface Science* 537 2019: pp. 66 – 78. https://doi.org/10.1016/j.jcis.2018.10.102
7. **Liu, J., Liu, A., Wang, W.** Feasibility of Nanoscale Zero-Valent Iron (nZVI) for Enhanced Biological Treatment of Organic Dyes *Chemosphere* 237 2019: pp. 124470. https://doi.org/10.1016/j.chemosphere.2019.124470
8. **Fatima, M., Farooq, R., Lindström, R.W., Saeed, M.** A Review on Biocatalytic Decomposition of Azo Dyes and Electrons Recovery *Journal of Molecular Liquids* 246 2017: pp. 275 – 281. https://doi.org/10.1016/j.molliq.2017.09.063
9. **Ma, J., Cui, B., Dai, J., Li, D.** Mechanism of Adsorption of Anionic Dye from Aqueous Solutions onto Organobentonite *Journal of Hazardous Materials* 186 2011: pp. 1758 – 1765. https://doi.org/10.1016/j.molliq.2017.09.063
10. **Wang, H., Zhong, Y., Yu, H.** High-efficiency Adsorption for Acid Dyes over $CeO_2 \cdot xH_2O$ Synthesized by A Facile Method *Journal of Alloys and Compounds* 776 2019: pp. 96 – 104. https://doi.org/10.1016/j.jallcom.2018.10.228
11. **Liu, S., Yang, Z., Chang, Y.** An Enzyme-Free Electrochemical Biosensor Combining Target Recycling with Fe_3O_4/CeO_2@Au Nanocatalysts for Microrna-21 Detection *Biosensors Bioelectronic* 119 2018: pp. 170 – 175. https://doi.org/10.1016/j.bios.2018.08.006
12. **He, H., Yang, P., Li, J.** Controllable Synthesis, Characterization, and CO Oxidation Activity of CeO_2 Nanostructures with Various Morphologies *Ceramics International* 42 2016: pp. 7810 – 7818. https://doi.org/10.1016/j.ceramint.2016.02.005
13. **Wu, M, Leung, D.Y.C., Zhang, Y.** Toluene Degradation over Mn-TiO_2/CeO_2 Composite Catalyst under Vacuum Ultraviolet (VUV) Irradiation *Chemical Engineering Science* 195 2019: pp. 985 – 994.

https://doi.org/10.1016/j.ces.2018.10.044

14. **Balaji, S, Mandal, B.K., Reddy, L.V.K., Sen, D.** Biogenic Ceria Nanoparticles (CeO_2 NPs) for Effective Photocatalytic and Cytotoxic Activity *Bioengineering (Basel)* 7 2020: pp. 214 – 233. https://doi.org/10.3390/bioengineering7010026
15. **Chen, J, Xiao, Y., Huang, B., Sun, X.** Sustainable Cool Pigments based on Iron and Tungsten Co-Doped Lanthanum Cerium Oxide with High NIR Reflectance for Energy Saving *Dyes and Pigments* 154 2018: pp. 1 – 7. https://doi.org/10.1016/j.dyepig.2018.02.032
16. **Zuas, O., Abimanyu, H., Wibowo, W.** Synthesis and Characterization of Nanostructured CeO_2 with Dyes Adsorption Property *Processing & Application of Ceramics* 8 (1) 2014: pp. 39 – 46. https://doi.org/10.2298/PAC1401039Z
17. **Wu, J., Wang, J., Du, Y.** Adsorption Mechanism and Kinetics of Azo Dye Chemicals on Oxide Nanotubes: A Case Study Using Porous CeO_2 Nanotubes *Journal of Nanoparticle Research* 18 2016: pp. 1 – 13. https://doi.org/10.1007/s11051-016-3497-8
18. **Liu, S.H., Yang, Z.H.** An Enzyme-free electrochemical Biosensor Combining Target Recycling with Fe_3O_4/CeO_2@Au Nanocatalysts for Microrna-21 Detection *Biosensors & bioelectronics* 119 2018: pp. 170 – 175. https://doi.org/10.1016/j.bios.2018.08.006
19. **Chang, J.L., Qing, L.** Synthesis of Fe_3O_4 Nanowire@CeO_2/Ag Nanocomposites with Enhanced Photocatalytic Activity under Sunlight Exposure *Ceramics International* 42 (10) 2016: pp. 11827 – 11837. https://doi.org/10.1016/j.ceramint.2016.04.104
20. **Cheng, Z., Liao, J., He, B.** One-Step Fabrication of Graphene Oxide Enhanced Magnetic Composite Gel for Highly Efficient Dye Adsorption and Catalysis *ACS Sustainable Chemistry & Engineering* 3 (7) 2015: 1677 – 1685. https://doi.org/10.1021/acssuschemeng.5b00383
21. **Gao, S.M., Zhou, H.P., Chen, D.H.** Magnetic Composite Fe_3O_4/CeO_2 for Adsorption of Azo Dye *Journal of Rare Earths* 2018: pp. 986 – 993. https://doi.org/10.1016/j.jre.2018.04.002
22. **Gao, S.M., Zhang, W.W., An, Z.H.** Adsorption of Anionic Dye onto Magnetic Fe_3O_4/Ceo_2 Nanocomposite: Equilibrium, Kinetics, and Thermodynamics *Adsorption Science & Technology* 3 (4) 2019: pp. 185 – 204. https://doi.org/10.1177/0263617418819164
23. **Deng, H., Li, X.L., Li, Y.D.** Monodisperse Magnetic Single-Crystal Ferrite Microspheres *Angewandte Chemie* 44 2005: pp. 2782 – 2785. https://doi.org/10.1002/anie.200462551
24. **Kong, Q., Wang, X., Lou, T.** Preparation of Millimeter-Sized Chitosan/Carboxymethyl Cellulose Hollow Capsule and Its Dye Adsorption Properties *Carbohydrate Polymers* 224 2020: pp. 1 – 31. https://doi.org/ 10.1016/j.carbpol.2020.116481
25. **Wang, P., Su, D., Zhang, S.N.** Constructing Mesoporous Phosphated Titanium Oxide for Efficient Cr(III) Removal *Hazard Mater* 384 2020: pp. 121278. https://doi.org/10.1016/j.jhazmat.2019.121278
26. **Dai, Y.M., Zou, J.Q., Liu, D.Y., Niu, L.L., Zhou, L.L., Zhou, Y., Zhang, X.H.** Preparation of Congo Red Functionalized Fe_3O_4@Sio_2 Nanoparticle and Its Application for the Removal of Methylene Blue *Colloids and Surfaces A: Physicochemical and Engineering Aspects* 550 2018: pp. 90 – 98. https://doi.org/10.1016/j.colsurfa.2018.04.033
27. **Venkataswamy, P., Rao, K.N., Jampaiah, D., Benjaram, M.R.** Nanostructured Manganese Doped Ceria Solid Solutions for CO Oxidation at Lower Temperatures *Catalysis Letters* 146 (162) 2015: pp. 2105 – 2118. http://dx.doi.org/10.1016/j.apcatb.2014.06.038
28. **Chhetri, B.P., Parnell, C.M., Wayland, H.** Chitosan-Derived NiO-Mn_2O_3/C Nanocomposites as Non-Precious Catalysts for Enhanced Oxygen Reduction Reaction *ChemistrySelect* 3 (3) 2018: pp. 922 – 932. https://doi.org/10.1002/slct.201702907
29. **Brigante, M., Schulz, P.C.** Adsorption of the Antibiotic Minocycline on Cerium (IV) Oxide: Effect of pH, Ionic Strength and Temperature *Microporous and Mesoporous Materials* 156 2012: pp. 138 – 144. https://doi.org/10.1016/j.micromeso.2012.02.033
30. **Channei, D., Inceesungvorn, B., Wetchakun, N.** Photocatalytic Activity under Visible Light of Fe-doped CeO_2 Nanoparticles Synthesized by Flame Spray Pyrolysis *Ceramics International* 39 2013: pp. 3129 – 3134. https://doi.org/10.1016/j.ceramint.2012.09.093
31. **Alkan, M., Doğan, M., Turhan, Y.** Adsorption Kinetics and Mechanism of Maxilon Blue 5G Dye on Sepiolite from Aqueous Solutions *Chemical Engineering Journal* 139 2008: pp. 213 – 223. https://doi.org/10.1016/j.cej.2007.07.080
32. **John, P.C., Noemí, Z.** Synthesis, Characterization and Application of Cross-Linked Chitosan/Oxalic Acid Hydrogels to Improve Azo Dye (Reactive Red 195) Adsorption *Reactive and Functional Polymers* 155 2020: pp. 104699. https://doi.org/10.1016/j.reactfunctpolym.2020.104699
33. **Thirunavukkarasu, A., Nithya, R.** Adsorption of Acid Orange 7 using Green Synthesized Cao/Ceo_2 Composite: An Insight into Kinetics, Equilibrium, Thermodynamics, Mass Transfer and Statistical Models *Journal of the Taiwan Institute of Chemical Engineers* 111 2020: pp. 44 – 62. https://doi.org/10.1016/j.jtice.2020.04.007
34. **Jawad, A.H., Abdulhameed, A.S.** Mesoporous Iraqi Red Kaolin Clay as an Efficient Adsorbent for Methylene Blue Dye: Adsorption Kinetic, Isotherm and Mechanism Study *Surfaces and Interfaces* 19 2020: pp. 1 – 30. https://doi.org/10.1016/j.surfin.2019.100422
35. **Chowdhury, A., Kumari, S., Khan, A.A., Hussain, S.** Selective Removal of Anionic Dyes with Exceptionally High Adsorption Capacity and Removal of Dichromate ($Cr2O7^{2-}$) Anion using Ni-Co-S/CTAB Nanocomposites and Its Adsorption Mechanism *Journal of Hazardous Materials* 385 2020: pp. 121602. https://doi.org/10.1016/j.jhazmat.2019.121602
36. **Hameed, B.H., Ahmad, A.A., Aziz, N.** Isotherms, Kinetics and Thermodynamics of Acid Dye Adsorption on Activated Palm Ash *Chemical Engineering Journal* 133 2007: pp. 195 – 203. https://doi.org/10.1016/j.cej.2007.01.032
37. **Hu, J., Deng, W., Chen, D.H.** Ceria Hollow Spheres as an Adsorbent for Efficient Removal of Acid Dye *ACS Sustainable Chemistry & Engineering* 5 2017: pp. 3570 – 3582. https://doi.org/10.1021/acssuschemeng.7b00396
38. **Zhang, Y., Shi, R., Yang, P.** Fabrication of Electronspun Porous Ceo_2 Nanofibers with Large Surface Area for Pollutants Removal *Ceramics International* 2016: pp. 14028 – 14035. https://doi.org/10.1016/j.ceramint.2016.06.009

39. **Sakkayawong, N., Thiravetyan, P., Nakbanpote, W.** Adsorption Mechanism of Synthetic Reactive Dye Wastewater by Chitosan *Journal of Colloid & Interface Science* 286 2005: pp. 36 – 42. https://doi.org/10.1016/j.jcis.2005.01.020

40. **Xu, C., Shi, S.** Electrospun SiO_2-MgO Hybrid Fibers for Heavy Metal Removal: Characterization and Adsorption Study of Pb(II) and Cu(II). *Journal of Hazardous Materials* 381 2020: pp. 120974.1381 – 120974.12. https://doi.org/10.1016/j.jhazmat.2019.120974

41. **Boudreault, P., Esteruelas, M.A.** Insertion of Unsaturated C–C Bonds into the O–H Bond of An Iridium (III)-Hydroxo Complex: Formation of Phosphorescent Emitters with an Asymmetrical β-Diketonate Ligand *Inorganic Chemistry* 59 (21) 2020: pp. 15877 – 15887. https://doi.org/10.1021/acs.inorgchem.0c02395

42. **Rives, V., Prieto, O.** Synergistic Effect in the Hydroxylation of Phenol over CoNiAl Ternary Hydrotalcites *Journal of Catalysis* 220 (1) 2003: pp. 161 – 171. https://doi.org/10.1016/S0021-9517(03)00245-8

43. **Bogart, J.A., Lewis, A.J., Medling, S.A.** Homoleptic Cerium (III) and Cerium (IV) Nitroxide Complexes: Significant Stabilization of the 4+Oxidation State *Inorganic Chemistry* 52 (19) 2013: pp. 11600 – 11607. https://doi.org/10.1021/ic401974t

44. **Dzhagarov, B.M., Lepeshkevich, S.V., Chaikovski, A.F.** Mechanism and Dynamics of the Photoinduced Fe–O_2 Bond Breaking in Oxyhemoglobin 63 2020: pp. 1359 – 1362. https://doi.org/10.1007/s11182-020-02178-1